SCIENCE CHINA
Earth Sciences

•RESEARCH PAPER•

September 2018 Vol.61 No.9: 1261–1278
https://doi.org/10.1007/s11430-017-9214-2

Seismic rock physical modelling for gas hydrate-bearing sediments

Xinxin LIU[1,2*], Xingyao YIN[2,3] & Xiwu LUAN[1,2]

[1] *Key Laboratory of Gas Hydrate, Ministry of Land and Resources, Qingdao Institute of Marine Geology, Qingdao 266071, China;*
[2] *Laboratory for Marine Mineral Resources, Qingdao National Laboratory for Marine Science and Technology, Qingdao 266071, China;*
[3] *School of Geosciences, China University of Petroleum (East China), Qingdao 266580, China*

Received September 11, 2017; revised April 12, 2018; accepted April 16, 2018; published online July 10, 2018

Abstract There are ambiguities and uncertainties in the recognition of gas hydrate seismic reflections and in quantitative predictions of physical information of natural gas hydrate reservoirs from seismic data. Rock physical modelling is a bridge that transforms the seismic information of geophysical observations into physical information, but traditional rock physics models lack descriptions of reservoir micro-structures and pore-filling materials. Considering the mineral compositions and pore micro-structures of gas hydrates, we built rock physical models for load-bearing and pore-filling gas hydrate-bearing sediments, describe the mineral compositions, pore connectivity and pore shape using effective media theory, calculated the shear properties of pore-filling gas hydrates using Patchy saturation theory and Generalized Gassmann theory, and then revealed the quantitative relation between the elastic parameters and physical parameters for gas hydrate-bearing sediments. The numerical modelling results have shown that the ratios of P-wave and S-wave velocities decrease with hydrate saturation, the P-wave and S-wave velocities of load-bearing gas hydrate-bearing sediments are more sensitive to hydrate saturation, sensitivity is higher with narrower pores, and the ratios of the P-wave and S-wave velocities of pore-filling gas hydrate-bearing sediments are more sensitive to shear properties of hydrates at higher hydrate saturations. Theoretical analysis and practical application results showed that the rock physical models in this paper can be used to calculate the quantitative relation between macro elastic properties and micro physical properties of gas hydrate-bearing sediments, offer shear velocity information lacking in well logging, determine elastic parameters that have more effective indicating abilities, obtain physical parameters such as hydrate saturation and pore aspect ratios, and provide a theoretical basis and practical guidance for gas hydrate quantitative predictions.

Keywords Gas hydrate, Rock physical modelling, Load-bearing gas hydrate, Pore-filling gas hydrate, Shear modulus, Pore micro-structure, Elastic parameter

Citation: Liu X, Yin X, Luan X. 2018. Seismic rock physical modelling for gas hydrate-bearing sediments. Science China Earth Sciences, 61: 1261–1278, https://doi.org/10.1007/s11430-017-9214-2

1. Introduction

Gas hydrates are widespread in seafloor sediments along continental margins and in permafrost regions (Kvenvolden, 1993; Chand et al., 2004), and they are important strategic energy and potential future energy resources (Dillon et al., 1993). Gas hydrate-bearing sediments usually exhibit higher P-wave and S-wave velocities compared to normally compacted, water-filled marine sediments. On marine seismic profiles, gas hydrates are usually associated with specific seismic responses such as bottom simulating reflectors (BSRs), blank zones and polarity reversals (Miller et al., 1991; Song et al., 2007). The seismic reflection characteristics are important bases for gas hydrate identification and have been widely used in the exploration of natural gas hydrates (Shipley et al., 1979; Song et al., 2002; Luan et al., 2008). The elastic and seismic characteristics strongly depend on micro-physical properties such as mineralogy, porosity and pore-filling materials. However, during the formation of gas hydrates, as affected by the geological

*Corresponding author (email: xxinl@126.com)

structure, pressure, temperature and other geological and geophysical conditions, gas hydrates distribute in sediments with different microstructures (Sava and Hardage, 2006; Hu et al., 2014), which lead to various acoustic, elastic, and AVO properties and then to ambiguities and uncertainties in quantitative predictions of natural gas hydrate reservoirs from seismic data (Holbrook et al., 1996; Liu et al., 2005). Quantitative knowledge is needed to more accurately translate seismic information into physical properties.

Rock physical modelling is an effective tool for understanding relations between geophysical measurements and rock properties (Yin and Liu, 2016). Rock physical models for gas hydrate-bearing sediments have been developed based on time-averaged equations that include two-phase equations, three-phase equations (Miller et al., 1991; Wood et al., 1994) and weighted equations (Lee et al., 1996; Lee and Collett, 2001) that weight the Wood and Wyllie equations; these equations are simple to implement and work well for primary pore-dominated rocks, but they lack strict a theoretical basis, and the weighting factor requires substantial data to be calibrated and constrained. Dvorkin and Nur (1993, 1996) proposed a cementation model for sediments with strong cementation, gas hydrates were supposed to cement at grain boundaries or wrap around the grains, and the intergranular hydrate cementation significantly increases the elastic modulus of the dry sediment frame, which leads to dramatic increments in the estimated velocity, even with a small amount of gas hydrate (Ecker et al., 1998). The effective media model treats hydrates as load-bearing grains (Helgerud et al., 1999; Sakai, 1999; Ecker et al., 2000), but the critical porosity of real sediments is difficult to determine, and the model is poorly suited for low-porosity cement rocks. The DEM model relates the elastic properties with porosity, mineral components, micro pore structure and hydrate saturation (Jakobsen et al., 2000), the Kuster-Toksöz model trades the mixture of hydrates and water as part of sediment frame and trades clay as a pore-filling material (Zimmerman and King, 1986), and the model is suitable for low-porosity sediments, but the errors of predicted S-wave velocities are large when the hydrate saturation is very low or very high. The Biot/Gassmann equation introduces frequency dependent parameters to describe the shear strain of the framework (Carcione and Tinivella, 2000), but VSP or experimental data are required to calibrate various empirical parameters. The DN model, which calculates the elastic parameters of hydrate sediments using contact theory and the Gassmann equation, has been successfully applied to unconsolidated marine sediments (Dvorkin and Prasad, 2001), but its application results for consolidated sediments are unsatisfactory.

The rock physics models have been used successfully in hydrate saturation estimations (Shankar and Riedel, 2011; Gao et al., 2012; Qian et al., 2016), velocity feature analyses (Wang et al., 2013; Qu et al., 2017; Liu et al., 2017), seismic characterization analyses (Wang et al., 2014; Bai et al., 2016), seismic inversions and reservoir predictions (Lu and McMechan, 2002; Westbrook et al., 2008). However, different models predict different hydrate saturations for the same gas hydrate-bearing sediment, and a model will have different prediction accuracies for different sediments (Chand et al., 2004). This is partly due to the fact that any of the rock physics models are based on certain assumptions and have different application conditions. On the other hand, the microscopic distribution of hydrates varies widely in different sedimentary environments, and the elastic properties of pure hydrate components also vary from region to region. Laboratory measurements have shown that the presence of gas hydrates and other solid pore-filling materials would increase the shear strength of sediments, and the increase in magnitude depends on the content of hydrates in the pores and on the contact relationship between the hydrates and solid particles (Winters et al., 2007). However, most of the rock physics models currently used for pore-filling gas hydrate-bearing sediments ignore the hydrate characteristic of non-zero shear modulus. Therefore, rock physics models that consider the microscopic distribution characteristics and shear properties of pore-filling hydrates need to be further studied.

Micromechanical models of gas hydrates mainly refer to the presence of hydrates in pores, contact or cement the solid grains (Ye and Liu, 2011). There are different classifications for the micromechanical models. Ecker et al. (1998) proposed three models: hydrates are deposited at grain contacts only, on enveloping grains and deposited away from grain contacts. Dai et al. (2004) proposed six models: cementing at grain contacts, grain coatings, supporting matrix/grains, pore-filling, matrix and inclusions, and nodules/fracture-fillings. Sava and Hardage (2006) proposed four models: load-bearing, pore-filling, thin layers of pure gas hydrates intercalated with unconsolidated sediments, and thin layers of disseminated, load-bearing gas hydrates intercalated with unconsolidated sediments. Among different micromechanical models, the three most commonly discussed are pore-filling, load-bearing and cementation models (Waite et al., 2009). The two mechanically extreme models are pore-filling and load-bearing models.

Gas hydrates deposit at sediment grain boundaries and grow into pore spaces, and they become part of the pore-filling materials (Figure 1b) and affect the bulk stiffness and conduction properties of pore-filling materials (Helgerud et al., 1999). This kind of gas hydrate has been observed during laboratory tests (Figure 1a; Tohidi et al., 2001; Kleinberg et al., 2003) and has been found in the Mallik permafrost site in Canada and the Nankai Trough offshore Japan (Dallimore et al., 1999; Winters et al., 1999). As the saturation of pore-filling hydrates grows higher, the hydrates may deposit as

load-bearing components (Figure 1c); they bridge neighbouring grains and become part of the solid matrix, reduce the bulk porosity and weaken the stiffness of the solid phase (Berge et al., 1999). Dutta and Dai (2009) showed that the hydrate saturation estimated from measured data using the effective media theory that treats gas hydrates as load-bearing components matches the results best for available data in the McKenzie Delta, Canada, Blake Ridge, Atlantic Coast, and Keathley Canyon, Gulf of Mexico.

In this paper, we propose our rock physical modelling methods for pore-filling and load-bearing gas hydrates, the mineral composition and microstructure of the pore system are described using effective elastic media theories, and the shear property of pore-filling hydrate are described using Patchy Saturation theory and generalized Gassmann's equations. We analyse the quantitative relationship between elastic parameters and physical parameters, including porosity, pore shape, hydrate saturation and properties of pore-filling materials, then apply the method to Priest's laboratory data (2005) to demonstrate the validity of the rock physical model, and finally apply the method to measured data in the Shenhu area to calculate reliable elastic parameters and demonstrate the capability of the method.

2. Methods

In this section, we focus on rock physical modelling of load-bearing and pore-filling gas hydrates. Emphasis is placed on the microstructure of the pore system and the shear properties of pore-filling materials, and the main process of the rock physical modelling consists of three steps, as shown in Figure 2: (1) mineral components are mixed uniformly to form solid mineral matrix, (2) dry pores are added into the matrix to form a dry sediment frame, and (3) pore-filling materials are filled into pores to form saturated sediments.

2.1 Mineral matrix

Waite et al. (2009) summarized the dominant characteristics of gas hydrate-bearing reservoirs and showed that hydrates have been found in reservoirs with sediment types ranging from clay and sand through gravel. In this paper, considering the lithology and mineral composition of gas hydrate-bearing sediments, the solid matrix is supposed to be a uniform mixture of clay, quartz, calcite, and other solid grains, there are also hydrate grains in matrix of load-bearing sediments. At any given volume fraction of solid components, the effective modulus of the solid mixture will fall between the Voigt and Reuss bounds (Mavko et al., 2009). The Hashin-Shtrikman bounds are the narrowest possible range without specifying geometric details of the constituents. A more general form of the Hashin-Shtrikman bounds was applied to mineral mixtures of more than two phases (Berryman, 1995):

$$K^{\mathrm{HS}\pm}=\left[\sum_{i=1}^{N} f_i/\left(K_i+4\mu^{\pm}/3\right)\right]^{-1}-4\mu^{\pm}/3, \tag{1}$$

$$\mu^{\mathrm{HS}\pm}=\left[\sum_{i=1}^{N} f_i/\left(\mu_i+\zeta^{\pm}\right)\right]^{-1}-\zeta^{\pm}, \tag{2}$$

where $\zeta^{\pm}=\mu^{\pm}(9K^{\pm}+8\mu^{\pm})[6(K^{\pm}+2\mu^{\pm})]^{-1}$; K^{+} and K^{-} are the maximum and minimum bulk moduli; μ^{+} and μ^{-} are the maximum and minimum shear moduli, respectively; and f_i, K_i and μ_i are the volume fraction, bulk modulus and shear modulus of the ith mineral component, respectively. For a load-bearing hydrate, the bulk porosity of the sediment is

$$\phi=\phi_{\mathrm{r}}(1-S_{\mathrm{gh}}), \tag{3}$$

where ϕ is the porosity after deposition of gas hydrates, ϕ_{r} is the original porosity, and S_{gh} is the saturation of the gas hydrate. The volumetric fraction of gas hydrate within the solid is

$$f_{\mathrm{gh}}=C_{\mathrm{gh}}/(1-\phi), \tag{4}$$

where C_{gh} is the volumetric fraction of the gas hydrate in the sediment.

2.2 Sediment frame

The microstructures of pore systems greatly impact the

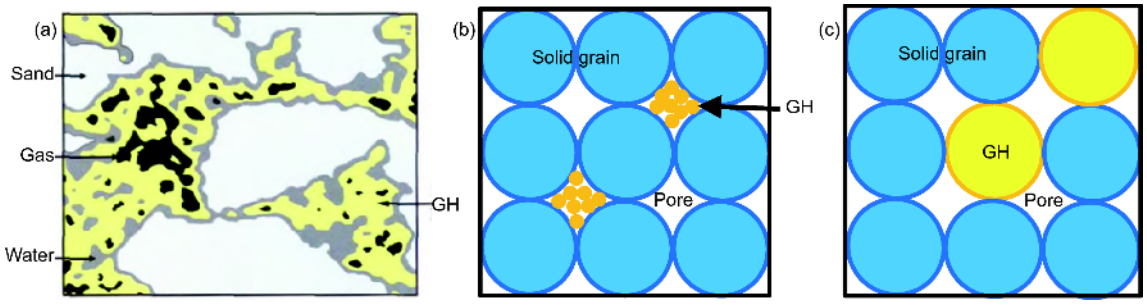

Figure 1 CT imagery and diagrams for the micro-distribution of gas hydrates. (a) X-ray Micro CT imagery in a laboratory-made sample (modified from Jin et al., 2006), we can see sand grains (white), gas (black), water (light grey) and hydrate (yellow, which is represented by GH in the figure); (b) configuration for pore-filling gas hydrates; (c) configuration for load-bearing gas hydrates.

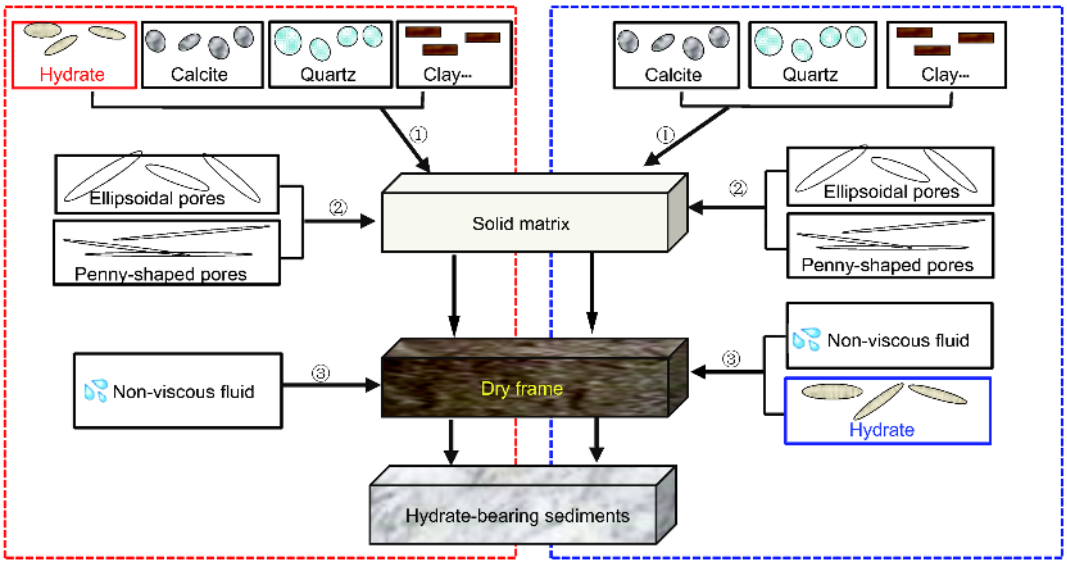

Figure 2 Diagram of the rock physical modelling method. The diagram in the left red box shows the rock physical modelling method for load-bearing gas hydrate-bearing sediments, and the diagram in the right blue box shows the rock physical modelling method for pore-filling gas hydrate-bearing sediments.

elastic moduli of gas hydrate-bearing sediments (Wang et al., 2016). Studies have shown that the presence of clay lowers pore aspect ratios (Xu and White, 1995), and the percentages of pore water bounded to clay particles increase as clay content increases (Lee and Waite, 2008). Pore shape has an important impact on the elastic properties of the reservoirs (Jiang, 2003; Weger et al., 2009). A variety of pore-shape-based reservoir pore system classification methods have been proposed (Bao, 1988; Dun, 1995). With reference to the previous pore system classification, this paper focuses on pore shape and connectivity and divides the microscopic pore system into two parts: poorly-connected penny-shaped pores with smaller aspect ratios and better-connected ellipsoidal pores with larger aspect ratios. The porosities of penny-shaped pores are proportional to clay volume fraction, and the porosities of ellipsoidal pores are proportion to the volume fractions of other solid components.

Add dry pores into a solid matrix to form a dry frame. The differential effective medium (DEM) theory equates the process of calculating the elastic parameters of a two-phase mixture to a process of adding inclusions incrementally to the matrix phase, and the coupled differential equations for the effective bulk and shear modulus are (Mavko et al., 2009)

$$(1-\phi)\frac{\mathrm{d}}{\mathrm{d}\phi}\left[\mathbf{K}_{\mathrm{d}}^{*}(\phi)\right]=\left(\mathbf{K}_{2}-\mathbf{K}_{\mathrm{d}}^{*}\right)\mathbf{P}^{*i}(\phi), \tag{5}$$

$$\mathbf{K}^{*}(0)=\mathbf{K}_{1}, \tag{6}$$

where $\mathbf{K}_{\mathrm{d}}^{*}=(K_{\mathrm{d}}^{*},\mu_{\mathrm{d}}^{*})$, K_{d}^{*} and μ_{d}^{*} are the effective bulk and shear moduli of the dry frame including inclusions, respectively, $\mathbf{K}_{1}$ and $\mathbf{K}_{2}$ are the elastic moduli of the of the initial host material and inclusions, respectively, the geometric coefficients $\mathbf{P}^{*i}=(P^{*i},Q^{*i})$, P^{*i} and Q^{*i} are functions of the content, shape and elastic modulus of the *i*th inclusion because both geometric coefficients are related to the bulk modulus and shear modulus of the dry framework, and the differential equations of bulk modulus and shear modulus are coupled. Yin et al. (2016) assumed that the modulus ratio of a dry frame is a linear function of porosity and decoupled the differential equations:

$$K_{\mathrm{d}}^{*}(\phi)=K_{1}(1-\phi)^{(P^{0}+P^{1})}e^{P^{1}\phi}, \tag{7}$$

$$\mu_{\mathrm{d}}^{*}(\phi)=\mu_{1}(1-\phi)^{(Q^{0}+Q^{1})}e^{Q^{1}\phi}, \tag{8}$$

where $P^{0}=\frac{A_1}{A_4}$, $P^{1}=\frac{A_2A_4-A_1A_5}{A_4^2}$, $Q^{0}=\frac{C_1}{C_4}+\frac{D_1}{D_4}$, $Q^{1}=\frac{C_2C_4-C_1C_5}{C_4^2}+\frac{D_2D_4-D_1D_5}{D_4^2}$, and $A_1,A_2,\ldots,A_5$, $C_1,C_2,\ldots,C_5$ and $D_1,D_2,\ldots,D_5$ are parameters that are related to the pore aspect ratio and elastic modulus of solid matrix; the detailed expressions are shown in Yin et al. (2016).

2.3 Saturated rock

For load-bearing gas hydrates, pore-filling materials are fluids including water, and/or gas, and they do not affect the shear properties of the sediments. The Gassmann equations compose the most frequently used method to calculate the elastic properties of isotropic homogeneous saturated rock filled with different fluids. The bulk modulus of the isotropic saturated rock can be expressed as (Gassmann, 1951)

$$K_{\mathrm{s}}=K_{\mathrm{d}}+\alpha^{2}K_{\mathrm{f}}\left[\phi+(\alpha-\phi)K_{\mathrm{f}}/K_{\mathrm{m}}\right]^{-1}, \tag{9}$$

$$\mu_{\mathrm{s}}=\mu_{\mathrm{d}}, \tag{10}$$

where $\alpha=1-K_{\mathrm{d}}/K_{\mathrm{m}}$, K_{s}, K_{d} and K_{m} are the bulk moduli of

the saturated rock, dry rock frame and rock matrix, respectively, μ_s and μ_d are the shear moduli of the saturated rock and dry rock frame, respectively. The shear modulus of saturated rock is the same as that of the dry rock frame.

For pore-filling hydrates, pore spaces are filled with hydrates, water or gas, the pore pressures produced by these materials differ from each other due to their different elastic properties, the solid-like characteristics (viscosity) of the hydrates may cause pore pressure imbalances across the whole pore space, and the sediments are then patchily saturated. Patches smaller than the critical relaxation scale will reach the equilibrium of the pore-filling phases, whereas adjacent patches larger than the critical relaxation scale will not be equilibrated with each other. Each patch will have a different effective bulk module, and the bulk modulus of saturated sediments can be expressed as follows (Hill, 1963):

$$K_R = \left\langle (K + 4\mu/3)^{-1} \right\rangle^{-1} - 4\mu/3, \tag{11}$$

where K_R is the equivalent bulk modulus of the patchy saturated sediments, and $\langle \cdot \rangle$ is the average over patches weighted by their volume fractions. Regarding shear modulus, each patch has a different effective pore-filling that is described approximately by the Reuss average:

$$\mu_R = \left(\sum_{i=1}^{N} f_i / \mu_i \right)^{-1}, \tag{12}$$

where μ_R is the equivalent shear modulus, and μ_i and f_i are the shear modulus and the volume fraction of the ith patch, respectively.

For patches filled with gases or other fluids, the pore pressure is easily balanced inside the patches, and the bulk modulus can therefore be expressed by the Gassmann equation. However, for sediments with solid pore-filling materials, the saturated shear modulus differs from the dry shear modulus. Ciz and Shapiro (2007) derived the elastic tensor of a solid-saturated porous rock by analysing the deformations of the rock frame and the pore-filling material subjected to confining and pore-space stresses:

$$S^{s}_{ijkl} = S^{d}_{ijkl} - \left(S^{d}_{ijkl} - S^{m}_{ijkl} \right) \times [\phi(S^{if} - S^{\phi}) + S^{d} - S^{m}]^{-1}_{mnqp} \left(S^{d}_{mnqp} - S^{m}_{mnqp} \right). \tag{13}$$

This equation is a more generalized form of the Gassmann equation that overcomes the conditions under which the Gassmann equation assumes that all pores are full of frictionless fluids. $\mathbf{S}^s$, $\mathbf{S}^d$ and $\mathbf{S}^m$ are compliance tensors of saturated patchy, dry patchy and solid matrix, respectively, and $\mathbf{S}^{if}$ is the compliance tensor of the pore-filling material. If the shear modulus of the pore-filling material is zero, then $\mathbf{S}^{if}$ degrades to the fluid compression coefficient, and eq. (13) degrades to Brown-Korringa fluid substitution equation in anisotropic rocks (Brown and Korringa, 1975). $\mathbf{S}^{\phi}$ is the compliance tensor related to pore space of the dry porous frame. For the isotropic frame, $\mathbf{S}^{\phi} = \mathbf{S}^m$ and eq. (13) can be expressed in terms of the elastic modulus:

$$K_s^{-1} = K_d^{-1} - \left(K_d^{-1} - K_m^{-1} \right)^2 \times \left[\phi \left(K_{if}^{-1} - K_{\phi}^{-1} \right) + \left(K_d^{-1} - K_m^{-1} \right) \right]^{-1}, \tag{14}$$

$$\mu_s^{-1} = \mu_d^{-1} - \left(\mu_d^{-1} - \mu_m^{-1} \right)^2 \times \left[\phi \left(\mu_{if}^{-1} - \mu_{\phi}^{-1} \right) + \left(\mu_d^{-1} - \mu_m^{-1} \right) \right]^{-1}, \tag{15}$$

where μ_s, μ_d and μ_m are the shear moduli of the saturated rock, dry rock frame and rock matrix, respectively, K_{ϕ} and μ_{ϕ} are the bulk and shear moduli related to the pore space of the rock frame, and K_{if} and μ_{if} are bulk and shear moduli of the ith solid pore-filling components. In the case of sediments with a single mineral component ($K_{\phi} = K_m$) and fluid pore-filing material ($\mu_{if} = 0$), eqs. (14) and (15) degrade to the Gassmann eqs. (9) and (10).

3. Numerical modelling

We analyzed the rock physical models described above for variations in elastic modulus, velocities and V_P/V_S with hydrate saturation, porosity, pore shape and pore-filling materials. The reference model is supposed to be comprised of quartz and clay, and the pore-filling material is water. The pore aspect ratio (PAR) of penny-shaped pores is supposed to be 0.04, and the PAR of ellipsoidal pores is 0.35. The elastic constants are given in Table 1. The results of the rock physical modelling are shown in Figures 3–9.

Both the P-wave (V_P) and S-wave (V_S) velocities increase

Table 1 Elastic constants of sediment constituents

Component	Bulk modulus (GPa)	Shear modulus (GPa)	Density (g cm^{-3})	Sources
Quartz	37.0	44.0	2.65	Carmichael, 1989
Clay	21.0	7.0	2.60	Tosaya and Nur, 1982
Gas hydrate	7.7	3.2	0.91	Waite et al., 2000
Water	2.25		1000	
Gas	0.00013		0.65	

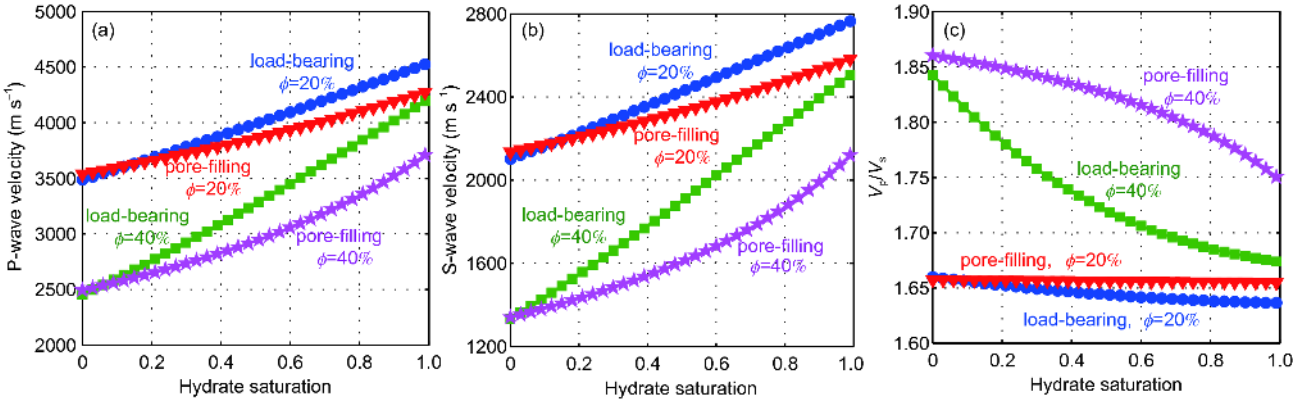

Figure 3 Velocities and V_P/V_S versus gas hydrate saturation for gas hydrate-bearing sediments. (a) V_P; (b) V_S; (c) V_P/V_S. ϕ represents porosity of gas hydrate-bearing sediments.

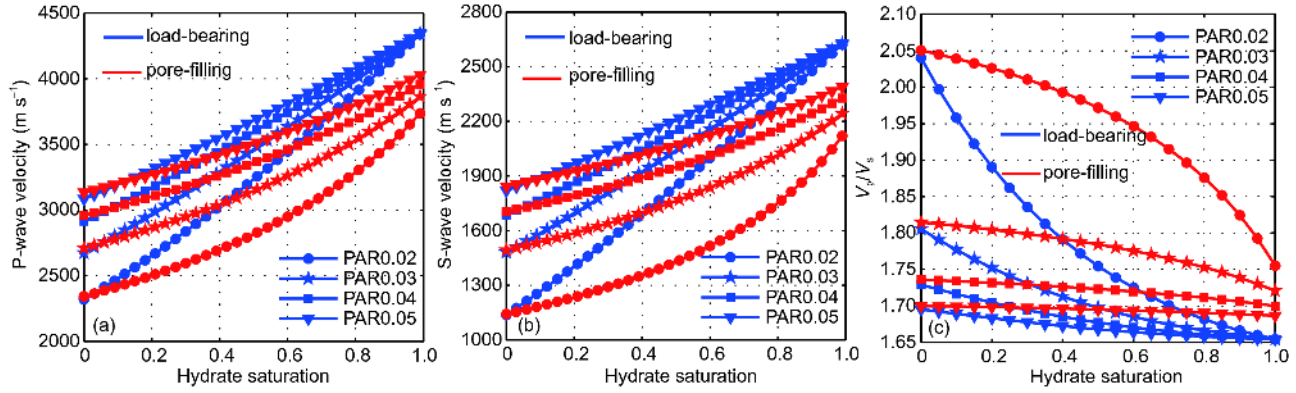

Figure 4 Velocities versus hydrate saturation for gas hydrate-bearing sediments with different PARs of penny-shaped pores. (a) V_P; (b) V_S; (c) V_P/V_S.

with hydrate saturation for load-bearing gas hydrate (LBGH)-bearing sediments and pore-filling gas hydrate (PFGH)-bearing sediments (Figure 3a and b). The velocities predicted by the LBGH model are higher than those predicted by the PFGH model when hydrate saturation exceeds 20%, and the incremental magnitude predicted by the LBGH model is larger than that predicted by PFGH model. From no hydrates up to 100% hydrate saturation, the relative increment in V_P predicted by the LBGH model is 30.1% when the porosity is 20% and 71.7% when the porosity is 40%, whereas those predicted by the PFGH model are 21.3% and 50.3%, respectively. The relative increment in V_S by the LBGH model is 31.9% when the porosity is 20% and 89.0% when the porosity is 40%, that for PFGH is 58.1%, and those predicted by the PFGH model are 20.9% and 57.7%, respectively. The velocities decrease with porosity for both models, which is similar to that of sediments without gas hydrates. The ratio of P-wave and S-wave velocities (V_P/V_S) decreases with porosity and hydrate saturation (Figure 3c), which is similar to Chand's (2004) results as predicted by four theories: weight equation, three-phase effective medium theory, three-phase Biot theory and DEM theory. For the same sediments, V_P/V_S predicted by the LBGH model is smaller than that of the PFGH model. When the porosity is 40%, V_P/V_S predicted by the LBGH model decreases rapidly at lower hydrate saturations and decreases slowly at higher hydrate saturations, whereas that of the PFGH model decreases slowly at lower hydrate saturations and decreases rapidly at higher hydrate saturations.

Both V_P and V_S increase while V_P/V_S decreases with PAR of penny-shaped pores (Figure 4). The incremental magnitudes of V_P and V_S are larger at smaller PAR. That is mainly because penny-shaped pores with smaller aspect ratios are easier to close when subjected to external forces and then have greater influences on velocities.

As hydrate saturation grows from 0 to 100%, the relative increment in V_P predicted by the LBGH model is 41.4% when the PAR of the penny-shaped pores is 0.05 and 88.2% when the PAR is 0.02; those predicted by the PFGH model are 29.0% and 60.8%, respectively. The relative increment in V_S predicted by the LBGH model is 44.9% when the PAR of penny-shaped pores is 0.05 and 132.1% when the PAR is 0.02; those predicted by the PFGH model is 30.0% and 87.9%, respectively. The velocities also increase with the PARs of ellipsoidal pores (Figure 5), and the variation trend is similar to that with the PARs of penny-shaped pores with

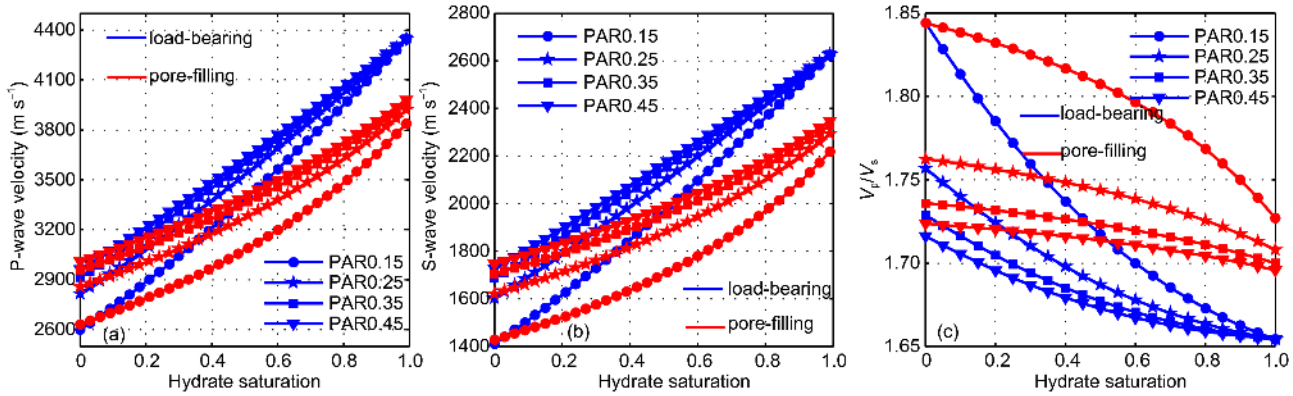

Figure 5 Velocities versus hydrate saturation for gas hydrate-bearing sediments with different PARs of ellipsoidal pores. (a) V_P; (b) V_S; (c) V_P/V_S.

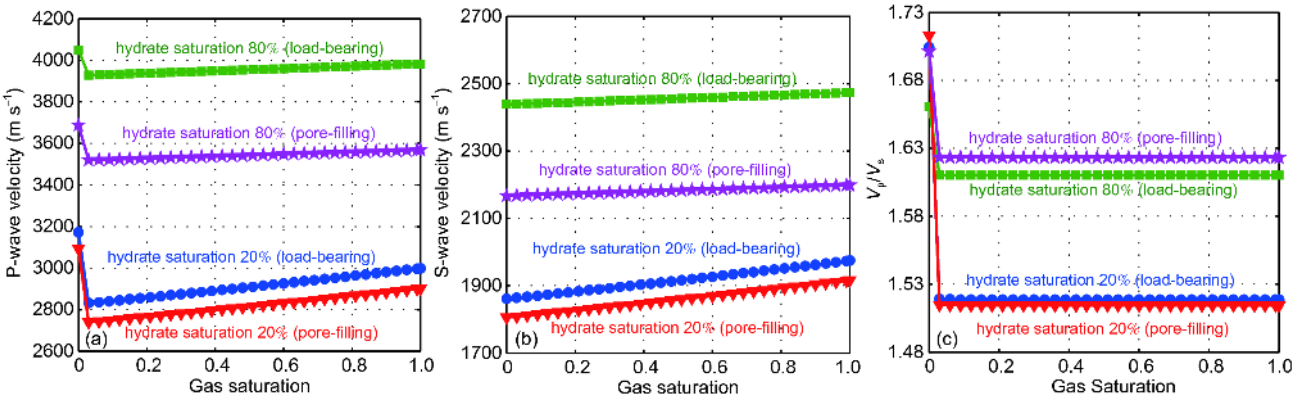

Figure 6 Velocities and V_P/V_S versus gas saturation at different gas saturations. (a) V_P; (b) V_S; (c) V_P/V_S.

different variation magnitudes. As hydrate saturation grows from 0 to 100%, the relative increment in V_P predicted by the LBGH model is 47.2% when the PAR of penny-liked pores is 0.45 and 67.7% when the PAR is 0.15, those predicted by the PFGH model are 32.7% and 46.6% respectively, the relative increment in V_S predicted by the LBGH model is 52.7% when the PAR of penny-liked pores is 0.45 and 87.0% when the PAR is 0.15, and those predicted by the PFGH model are 34.9% and 56.5%, respectively. This also shows that the S-wave velocity of the LBGH model is more sensitive to hydrate content. When PAR is smaller, V_P/V_S is more sensitive to hydrate content and decreases more rapidly

Both V_P and V_P/V_S are very sensitive to the presence of free gas (Figure 6), they decrease dramatically once there is small amount of free gas in the pore space, and V_P then increases slightly with increasing gas saturation. V_S increases slowly with gas saturation as a result of decreasing density. Once a small amount of gas enters the pore space, V_P/V_S predicted by the PFGH model decreases 11.6% at 20% hydrate saturation and 4.6% at 80% hydrate saturation, and that predicted by the PFGH model decreases 10.9% and 3.0%, respectively, which means the V_P/V_S predicted by the PFGH model is more sensitive to the presence of gas.

Gas hydrates are ice-like crystalline solids comprised of water molecules surrounding a gas molecule, and the structure can be divided into type I, type II, type H and type T, among which "Structure I" is the most common form of natural gas hydrate. The compositions and the occupancy rates in the cages for different structures are variable, and the changes in structure result in different properties of natural gas hydrates (Lu et al., 2007). Table 2 lists several of the most cited elastic constants of natural gas hydrates in different study areas. For sediments deposits with pore-filling hydrates, the compressibility of the sediment frame and saturated sediment are not affected by the hydrates, whereas the shear properties of saturated sediments are close related to pore-filling hydrates. For sediment deposits with load-bearing hydrates, the compressibility and shear modulus of the sediment frame all relate to the shear properties of the hydrates.

The bulk modulus predicted by the PFGH model almost remains unchanged, whereas that predicted by the LBGH model increased with the shear modulus of natural gas hydrates (Figure 7). The shear modulus, V_P and V_S predicted by both models all increase. The increases in magnitudes of the LBGH model are larger than those of the PFGH model. For

Table 2 Most cited elastic constants of gas hydrates

Bulk modulus (GPa)	Shear modulus (GPa)	Density (g cm^{-3})	Sources	Work area
5.6	2.4	0.767	Ecker, 2001	Blake Outer Ridge
6.41	2.54	0.91	Lee and Collett, 2001	Mallik 2L-38 well
7.7	3.2	0.91	Waite et al., 2000	laboratory experiments
7.9	3.3	0.9	Helgerud et al., 1999	ODP164, Site 995
8.7	3.5	0.92	Shankar and Riedel, 2011	Krishna-Godavari basin
8.41	3.54	0.925	Helgerud et al., 2009	laboratory experiments

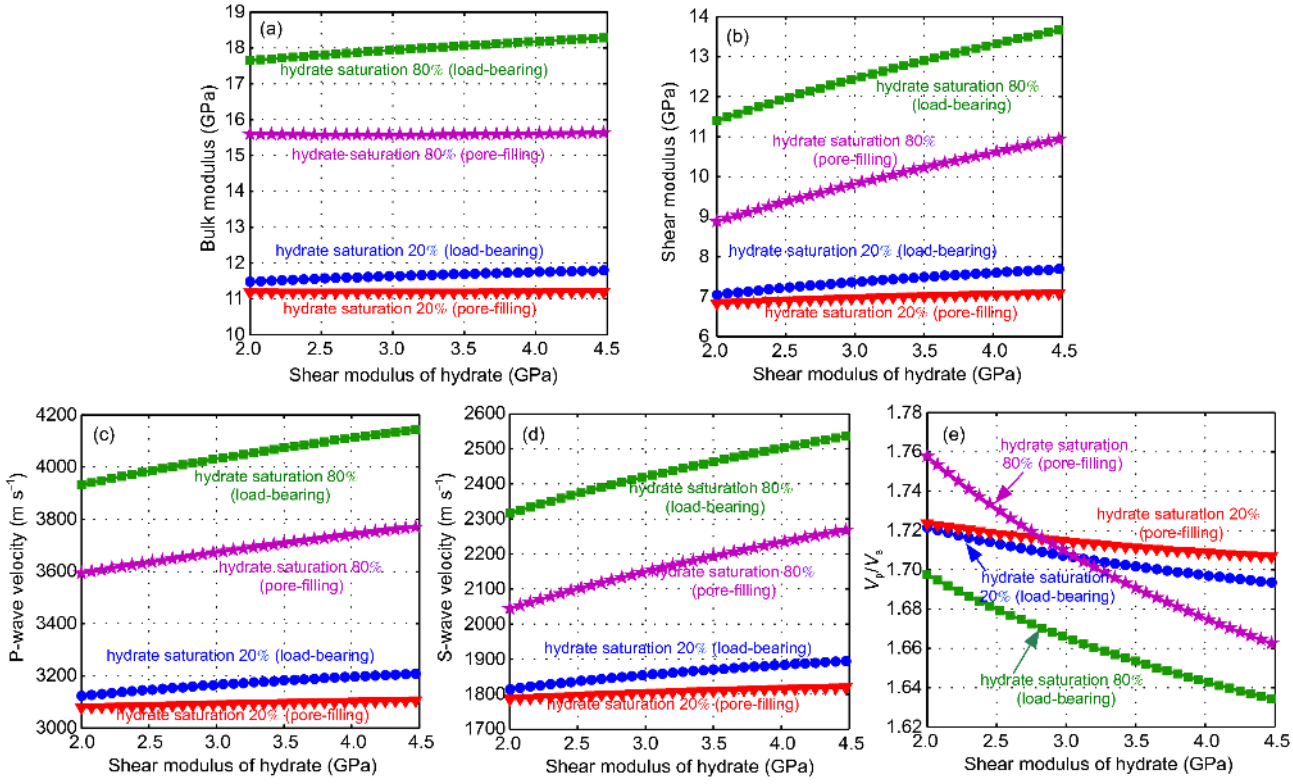

Figure 7 Elastic moduli, velocities and V_P/V_S versus shear modulus of hydrate at different hydrate saturations. (a) Bulk modulus; (b) shear modulus; (c) V_P; (d) V_S; (e) V_P/V_S.

hydrate saturations of 20% and 80%, as the shear modulus of hydrate increases from 2 to 4.5 GPa, the increments in V_P predicted by the LBGH model are 2.76% and 5.42%, respectively, and the increments of V_S are 4.46% and 9.50%, respectively; the increments in V_P predicted by the PFGH model are 0.86% and 4.91%, respectively, and the increments of V_S are 1.85% and 10.93%, respectively.

V_P/V_S predicted by the LBGH model decreases rapidly at lower hydrate saturations, whereas V_P/V_S predicted by the PFGH model decreases more rapidly at higher hydrate saturations. As the shear modulus of the hydrate increases from 2 to 4.5 GPa, for hydrate saturations of 20% and 80%, the decreases in V_P/V_S predicted by the LBGH model are 1.63% and 3.73%, respectively, whereas those predicted by the PFGH model are 0.98% and 5.42%, respectively.

Figures 8 and 9 are crossplots of elastic parameters, from which we can see the different sensitivities of elastic parameters to hydrate saturation. The combination of elastic parameters $\lambda\rho$ and $\mu\rho$ can well characterize the lithology and fluid characteristics of the sediments (Yin et al., 2015). The values of both $\lambda\rho$ and $\mu\rho$ increase with hydrate saturation, but for LBGH sediments, however, in the crossplot of $\lambda\rho$ and $\mu\rho$ (Figure 8b), samples with lower hydrate saturations and 30% porosity are overlapped with samples with higher hydrations and 40% porosity, primarily due to the much greater influence of porosity than the influence of pore fluids on the elastic properties of saturated sediments; that overlap may cause interpretation pitfalls. The following indicator is used to express the indicating ability of elastic parameters to hydrate saturation:

$$S_i = \left| \frac{P_i - P_0}{P_0} \right|, \tag{16}$$

where S_i is the indicator for formations when the hydrate

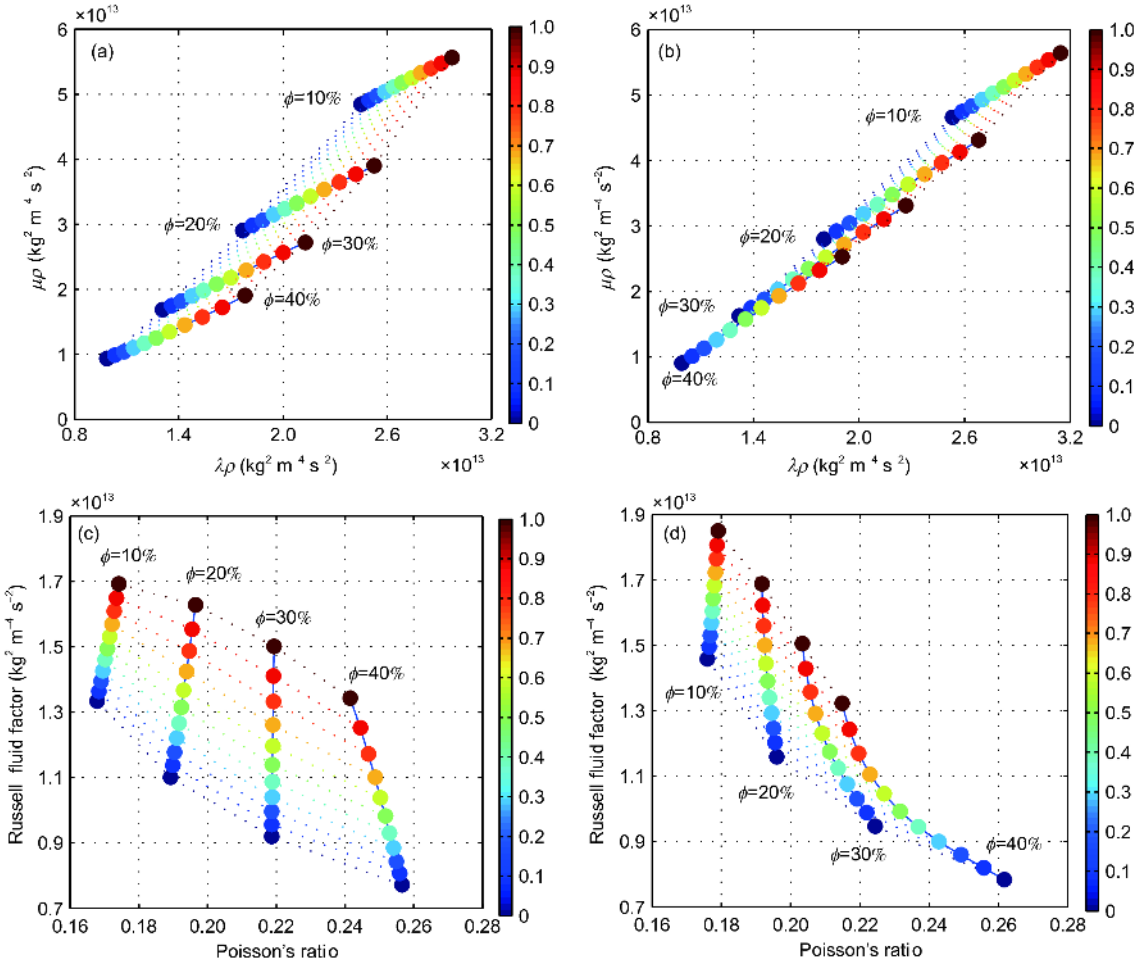

Figure 8 Crossplots of elastic parameters. (a) Crossplot of $\lambda\rho$ and $\mu\rho$ for PFGH formation; (b) crossplot of $\lambda\rho$ and $\mu\rho$ for LBGH formation; (c) crossplot of Poisson's ratio and Russell fluid factor for PFGH formation; (d) crossplot of Poisson's ratio and Russell fluid factor for LBGH formation. ϕ is sediment porosity, and the colour bars to the rights of the crossplots represent hydrate saturation.

saturation is i, P_i is the elastic parameter when the hydrate saturation is i, and P_0 is the elastic parameter for water saturated formations (the hydrate saturation is 0). We can see from Figure 9a and b that $\lambda\rho$ and $\mu\rho$ have better indicating abilities to hydrate saturation at higher porosities, the indicating ability of $\lambda\rho$ is almost the same for both models, the indicating ability of $\mu\rho$ is better than that of $\lambda\rho$ and becomes significantly stronger at higher porosities for LBGH formations.

Poisson's ratio is an elastic parameter that expresses the ratio of lateral compression and longitudinal extension and is closely related to V_P/V_S. For low-porosity formations, Poisson's ratio increases with increasing hydrate saturation, and the indicating ability of Poisson's ratio for PFGH formations is slightly greater than that for LBGH formations (Figure 9c). For high-porosity formations, Poisson's ratio decreases with increasing hydrate saturation, this phenomenon is particularly evident for LBGH formations, and the indicating ability of Poisson's ratio for LBGH formations is much greater. The Russell fluid factor is an elastic parameter that can reflect the pore fluid type; it is derived by rewriting the velocity equations under saturated fluid conditions based on the Biot-Gassmann theory and separating the modulus information of the dry frame and pore fluid (Russell et al., 2003). Because the hydrate components in both models all affect the shear properties of the formation, the Russell fluid factor can discriminate the hydrate saturation to a certain degree for the two micromechanical models, and we can see that the indicating ability of the Russell fluid factor to hydrate saturation is similar for the two models (Figure 9d).

4. Application to laboratory data

Priest et al. (2005) developed a gas hydrate resonant column (GHRC), and hydrates in the form of triply distilled, sieved, ground ice were added evenly into the pore spaces of air dried frozen sand under temperature and pressure conditions suitable for hydrate formation. The resulting moist sand was then tamped within a sample mold to form a dense solid

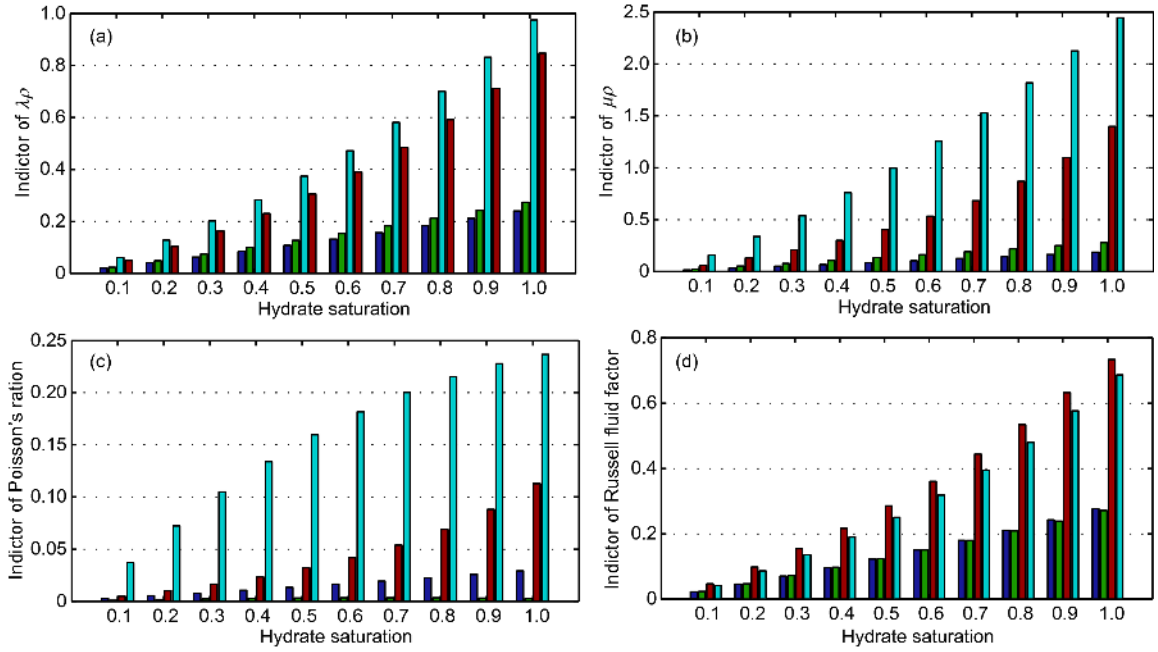

Figure 9 Indictor of elastic parameters for hydrate saturation. (a) $\lambda\rho$; (b) $\mu\rho$; (c) poisson's ratio; (d) russell fluid factor. The four bars corresponding to each hydrate saturation value from left to right represents PFGH formations with 10% porosity, LBGH formations with 10% porosity, PFGH formations with 40% porosity and LBGH formations with 40% porosity, respectively.

cylindrical specimen. During the measurement program, torsional and flexural resonance frequencies were measured at each loading (250 kPa up to 2000 kPa) and unloading (following the reverse sequence of loading) step. After calculation and correction of the measured data, the P-wave and S-wave velocities of thirteen specimens were obtained, and water-saturated P-wave velocities were also calculated using the Gassmann equation (Figure 10). Priest et al. (2005) also presented a conceptual model of the distribution for hydrate formation; initially, no hydrate was present (specimens H0L and H0D), and as hydrate grew into the pore spaces, at hydrate saturations less than 3%, partial cementation occurred with insufficient hydrate present to saturate all grain contacts, which is treated as load-bearing hydrates in this paper (specimens H1 and H2). For hydrate saturations exceeding 3%, the hydrate distribution was partially saturated or saturated in the pore spaces, which is treated as pore-filling hydrates in this paper.

We used the rock physics modelling methods proposed in Section 2 to calculate the velocities of the thirteen specimens. The bulk moduli of hydrate, quartz sand and water are 7.7, 36.6 and 2.25 GPa, respectively, which are the same as

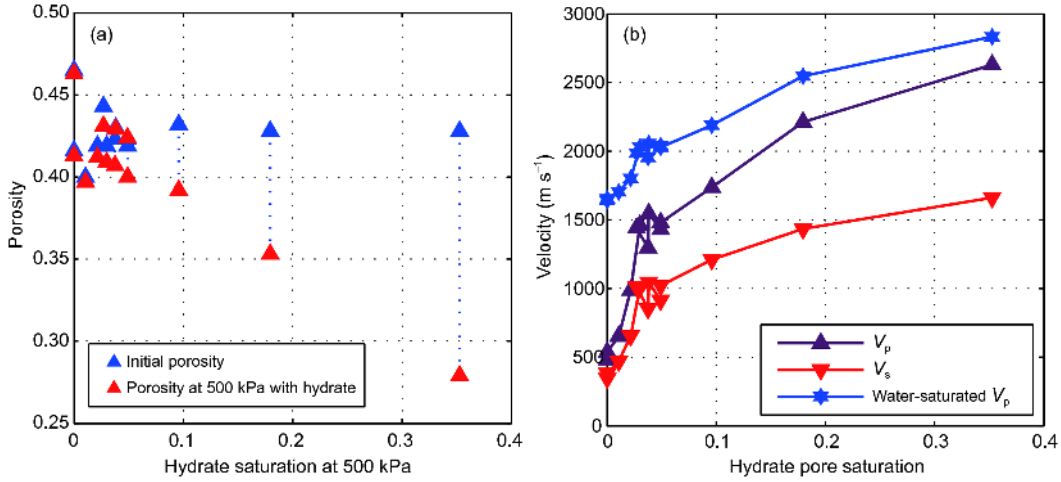

Figure 10 Properties and experimental results for thirteen specimens. (a) Hydrate saturation and porosity; (b) measured velocities with an effective confining pressure of 500 kPa. The P-wave velocity and S-wave velocity are measured when pore-filling materials are hydrate and free gas (dry specimens), and water saturated P-wave velocity is calculated after gas-water substitution.

those used by Priest et al. (2005). The shear modulus of the hydrate is 3.2 GPa (following Waite et al., 2000), that of quartz sand is 45 GPa (following Mason, 1943; he also used 36.6 GPa for the bulk modulus of quartz). Ellipsoidal pores are used to equivalently describe the pore space; however, the PAR is unknown. The rock physics model can build the quantitative relation between the physical parameters and velocities, so we used measured velocities to obtain the unknown physical parameters (Li et al., 2009; Xue et al., 2016). We inverted the PAR parameters using the measured P-wave and S-wave velocities and built the following objective functions:

$$E(\alpha_{\mathrm{P}}) = \min\left\| V_{\mathrm{lf}}^{\mathrm{M}} - V_{\mathrm{lf}}^{\mathrm{E}}(\mathbf{K};\mathbf{U};\phi;f_{\mathrm{s}};S_{\mathrm{gh}};\rho)\right\|, \quad (17)$$

$$E(\alpha_{\mathrm{S}}) = \min\left\| V_{\mathrm{S}}^{\mathrm{M}} - V_{\mathrm{S}}^{\mathrm{E}}(\mathbf{K};\mathbf{U};\phi;f_{\mathrm{s}};S_{\mathrm{gh}};\rho)\right\|, \quad (18)$$

where α_{P} and α_{S} are the PARs inverted from the measured V_{P} and V_{S}, respectively; $V_{\mathrm{lf}}^{\mathrm{M}}$ and $V_{\mathrm{S}}^{\mathrm{M}}$ are the measured P-wave and S-wave velocities, respectively; $V_{\mathrm{lf}}^{\mathrm{E}}$ and $V_{\mathrm{S}}^{\mathrm{E}}$ are the calculated P-wave and S-wave velocities, respectively; $\mathbf{K} = (K_{\mathrm{s}}, K_{\mathrm{gh}})$ and $\mathbf{U} = (\mu_{\mathrm{s}}, \mu_{\mathrm{gh}})$ are the bulk modulus and shear modulus of the solid compositions (quartz and hydrate); ϕ is the porosity of the specimens; f_{s} is the volume fraction of quartz; ρ is density; and S_{gh} is hydrate pore saturation. The objective functions are nonlinear equations, and we sought their minimum values using a genetic algorithm. The results are shown in Figure 11.

For each specimen, there is good agreement between the two PAR parameters calculated from the measured P-wave and measured S-wave velocities, which also illustrates the effectiveness of the method. The PARs of specimens H0L, H0D, H1 and H2 are smaller than those of the other nine specimens, primarily because the four specimens were not restricting load-bearing gas hydrate-bearing sands. The average PAR of specimens H0L, H0D, H1 and H2 calculated from measured P-wave velocity is 0.0629, and that calculated from the measured S-wave velocity is 0.0576. The average PAR for the other nine specimens calculated from the measured P-wave velocity is 0.0843, and that calculated from the measured S-wave velocity is 0.0840. Finally, we chose 0.060 as the PAR for H0L, H0D, H1 and H2, 0.084 as the PAR of the other nine specimens and then calculated the water-saturated velocities (Figure 12a).

The correlation coefficient of the calculated value and Priest's result is 0.96 for the P-wave velocity and 0.94 for the S-wave velocity, and the relative errors for the P-wave and S-wave velocities are 6.2% and 12.2%, respectively. The calculated $V_{\mathrm{P}}/V_{\mathrm{S}}$ agree well with Priest's result for specimens H3-1–H40 (Figure 12b). We then inverted the hydrate saturation using the calculated P-wave and S-wave velocities, and the relative error of inversed and measured value is 12.3% (Figure 12c). The results verify the validity and effectiveness of the rock physical models.

5. Application to real data

In 2007, gas hydrate drilling was carried out in the Shenhu area by the Guangzhou Marine Geological Survey and eight sites were drilled. The recovered core samples from wells SH2, SH3 and SH7 contained gas hydrates. At site SH2, the well logs include resistivity, natural gamma ray, P wave velocity, and density, as shown in Figure 13. The acoustic travel-time decreases significantly in the hydrate layer, which means that P-wave velocity increases significantly. The chloride concentration showed that the depth of the gas hydrate-bearing layer is 195–220 mbsf, the thickness is approximately 25 m, and the hydrate saturation averaged 25%, with a maximum value up to 45%. The highest value is 48%,

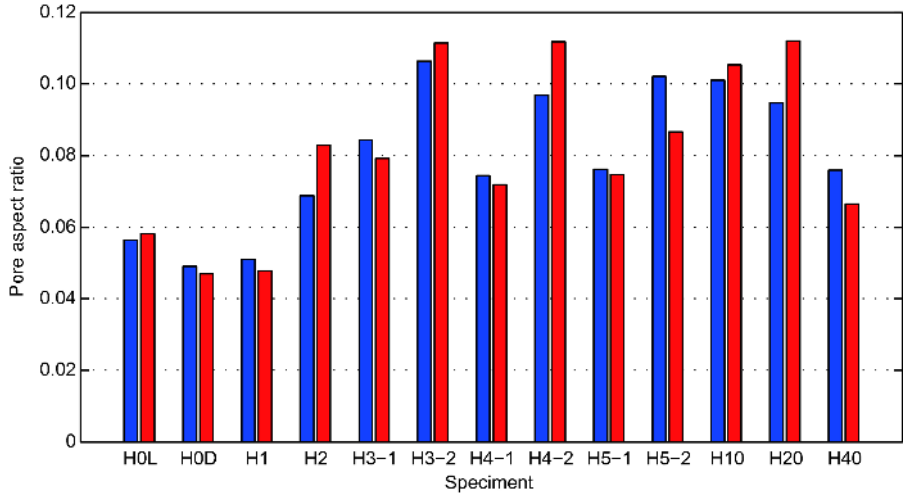

Figure 11 PAR inverted from the measured velocities for thirteen specimens. The blue and red bars represent the PARs inverted for the measured P-wave and S-wave velocities, respectively.

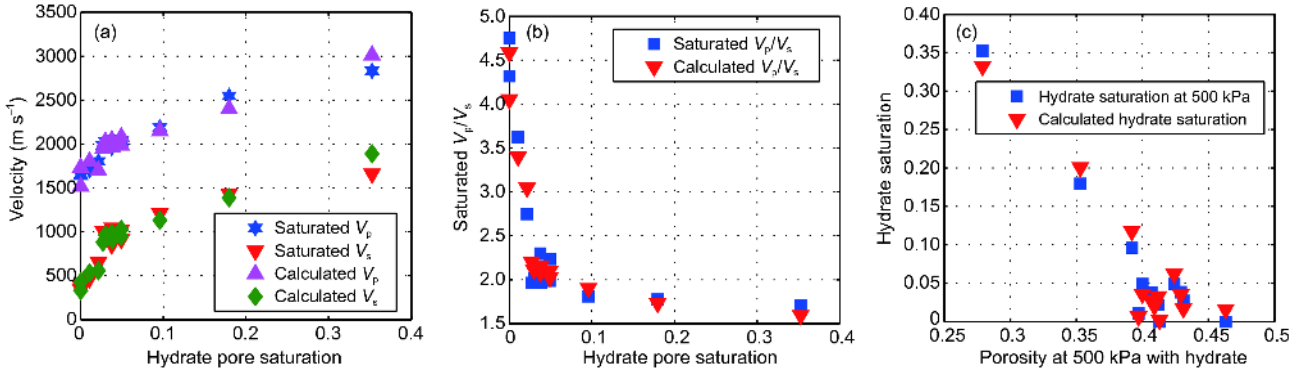

Figure 12 Calculated results for thirteen sand specimens. (a) Water-saturated V_P and V_S; (b) water-saturated V_P/V_S; (c) inversed hydrate saturation from calculated V_P and V_S.

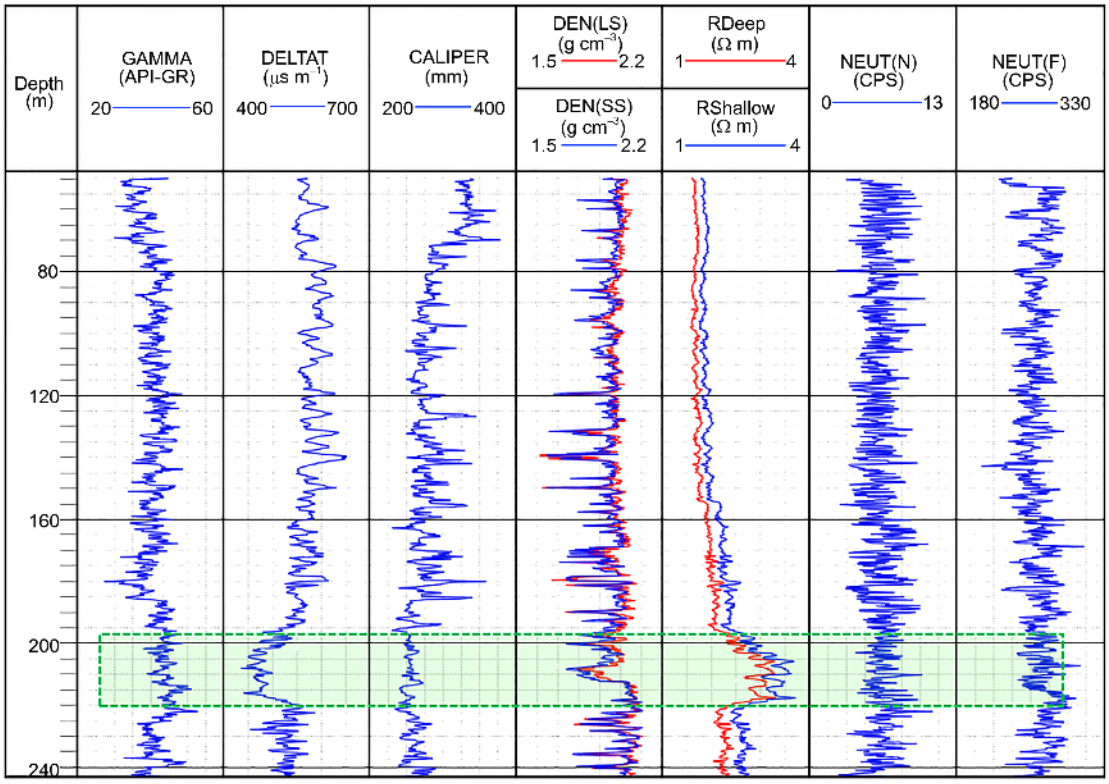

Figure 13 Measured well log data at site SH2. The well log curves rom left to right are gamma ray, acoustic travel-time, borehole diameter, density, resistivity, and neutron logging. The dotted green box represents the hydrate layer.

which is obviously higher than the diffusion hydrate saturation of less than 7% that is considered by international tradition theory. This is related to the unique gas hydrate geological system, including the structural fissures, fractures, pore spaces, and gas source types in the Shenhu area (Wu et al., 2009). The hydrates in this area are uniformly distributed in the pores among the sediment particles (Schultheiss et al., 2009). The seismic rock physical model of pore-filling gas hydrates was used to approximate the micromechanical model of hydrates at site SH2 in this area.

An X-ray diffraction analysis of the core samples indicates that the mineral components are mainly comprised of clastic, clay and carbonate minerals, and there are small amounts of magnesite, goethite, hematite, sepiolite, and halite in some of the layers. The detrital minerals are mainly quartz, plagioclase, orthoclase, muscovite, amphibole and pyrite. The content of quartz in SH2 is 19.0–39.4% and averages 28.26%, the content of muscovite is 10.5–30.1% and averages 19.57%, and the content of plagioclase is 4.8–12.6%, with an average of 8.13%. Compared with adjacent layers, the content of terrigenous clastic minerals such as hydrates, quartz and feldspar was relatively high at ap-

proximately 40%. The clay minerals are dominated by illite, chlorite, kaolinite and montmorillonite, and their contents range from 11.3% to 27.3% and average 19.64%. The carbonate minerals are dominated by calcite, the contents of which range over 8.8–37.3% and average 16.46%, a small amount of dolomite and ankerite was found in some layers, and in the hydrate layers, carbonate content is very low at approximately 12% (Lu et al., 2009). In general, the hydrate layers have small changes in mineral composition and content. The hydrates in this area are typical 'Structure I' and have methane gas contents above 99.3% (Liu et al., 2012). The modulus and density parameters used are shown in Table 3, in which the specific composition of the mineral mixture is quartz 28.0%, feldspar 12.0%, mica 26.0%, clay 20.0% and calcite 14.0% (Wang et al., 2011).

The input parameters, including porosity and gas hydrate saturation, were calculated from the measured well logs. The porosity was calculated from density:

$$\phi = \frac{\rho_m - \rho_b}{\rho_m - \rho_w}, \tag{19}$$

where ρ_b is the bulk density, ρ_w is the density of water, for which we use a value of 1030 kg m^{-3} in this paper, and ρ_m is the matrix density, which has a value of 2650 kg m^{-3}. The calculated porosities are shown in Figure 14a.

In the exploration of natural gas hydrates, Archie equation is a basic formula used to estimate hydrate saturation from resistivity logging data (Chen et al., 2013). In this paper, hydrate saturation is calculated from resistivity using the Archie equation (Wang et al., 2011):

$$S_h = 1 - \left(\frac{aR_w}{\phi^m R_t}\right)^{\frac{1}{n}}, \tag{20}$$

where R_w and R_t are the resistivities of the connate water and gas hydrate-bearing sediments, respectively, a, m and n are Archie constants, and the input parameters for the Archie equation are a=1.3 and m=n=2.0 in this paper.

The pore system microstructure consists of penny-shaped pores and ellipsoidal pores. Using the measured P-wave velocity to calculate the aspect ratios of the two kinds of pores, the objective function is established as

$$E(\alpha_p, \alpha_e) = \left\| V_P^M - V_P^E(\mathbf{K};\mathbf{U};\mathbf{F};\mathbf{\Phi};\rho;S_{gh}) \right\|, \tag{21}$$

where α_p and α_e are the aspect ratios of the penny-shaped pores and ellipsoidal pores, respectively; V_P^M and V_P^E are the measured and calculated P-wave velocities, respectively; $\mathbf{K} = (K_1, K_2, \ldots, K_N)$ and $\mathbf{U} = (\mu_1, \mu_2, \ldots, \mu_N)$ are the bulk and shear moduli of the mineral components, respectively; $\mathbf{F} = (f_1, f_2, \ldots, f_N)$ is the volume fraction for each of the components; $\mathbf{\Phi} = (\phi_p, \phi_e)$ are the porosities for the penny-shaped pores and ellipsoidal pores, respectively; S_{gh} is the hydrate saturation; and ρ is the formation density.

Table 3 Elastic moduli and densities of minerals for site SH2[a)]

Components	Bulk modulus (GPa)	Shear modulus (GPa)	Density (kg m^{-3})
Methane hydrate (5 MPa, 273 K)	8.41	3.54	0.922
Methane gas (10 MPa, 273 K)	0.015	0	90
Mineral mixture	45.27	26.0	2.667

a) Data sources: Wang et al., 2011

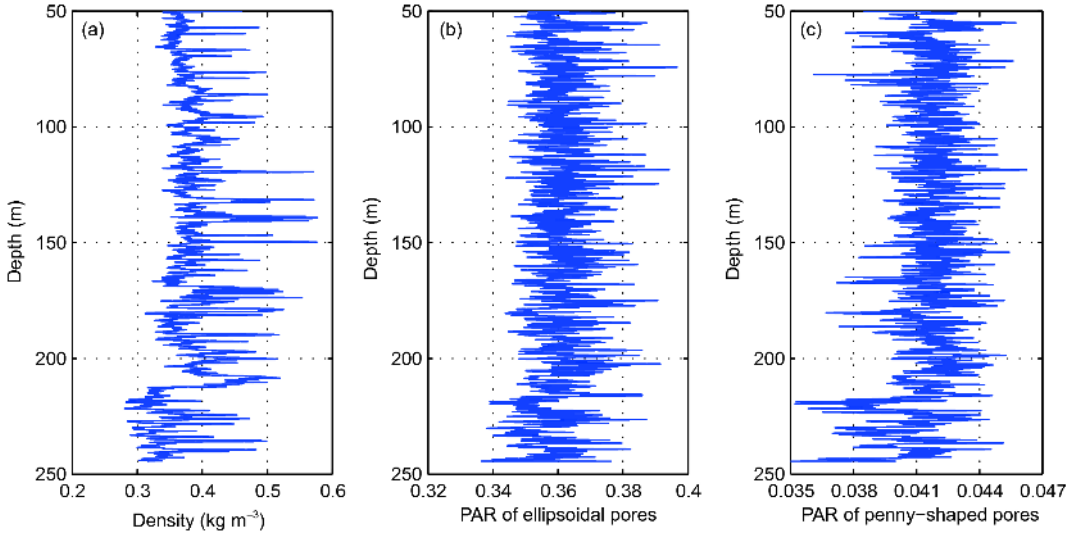

Figure 14 Calculated porosity and pore aspect ratios. (a) Porosity calculated from density; (b) aspect ratio of ellipsoidal pores; (c) aspect ratio of penny-shaped pores.

To obtain the pore aspect ratio parameters, we should seek the minimum value of the objective function (21). The process is to solve a nonlinear and multivariable function, for which we used the adaptive genetic algorithm. The algorithm uses the information of the objective function itself to establish the optimization direction and has the global optimality. The initial values were set to 0.3 and 0.04. In order to reduce the multiplicity, two hard constraints are added: first, the Poisson's ratio should fall within the interval (0,0.5), and second, the bulk modulus of the formation must fall within the Voigt-Ruess bounds. The results are shown in Figure 14b and c. The averaged PAR of ellipsoidal pores for the hydrate layer is 0.361, the PAR of the penny-shaped pores is slightly higher in the hydrate layer than in the surrounding layers, which is 4.16×10^{-2}, and the two PARs of the surrounding layers are 0.360 and 4.11×10^{-2}, respectively. Using the calculated PARs, the P-wave velocity and Poisson's ratio for site SH2 were calculated, the results of which are shown in Figure 15.

The calculated V_P agrees well with the measured values, especially for the low frequency trend, the correlation coefficient of the calculated and measured P-wave velocities is 0.9, the variance is 0.0178, the average absolute error is 45.99 m s^{-1}, the relative errors follow normal distribution approximately (Figure 16) and the average relative error is 2.26%. Poisson's ratio calculated from the calculated V_P and calculated V_S are consistent with that calculated from measured V_P and calculated V_S in the low frequency trend but has a wider range of variation. There are two main reasons for this phenomenon: (1) the input parameters associated with the pore microstructure, including the PARs of the penny-shaped pores and ellipsoidal pores, were calculated from measured data without calibration by core analysis or laboratory data, and (2) there are abundances of calcareous fossils and foraminifera at site SH2; these two mineral components have larger particles and increase the size and roundness of pore spaces (Wang et al., 2011), which lead to uncertainties in the elastic moduli of the minerals used in this paper and the variation in PAR. We inverted the hydrate saturation using the calculated V_P, the results of which are shown in Figure 15d, the inversed values agree very well with those calculated using the Archie equation.

The analysis of the crossplots of the calculated elastic parameters shows that only the measured natural gamma data and P-wave velocity data have limited ability to indicate different hydrate contents, whereas the crossplots of Poisson's ratio and P-wave velocity provide better indications (Figure 17). At locations with higher hydrate contents in the hydrate layer of site SH2, the P- and S-wave velocities are relatively high, the Poisson's ratios are relatively low, the $\lambda\rho$ are relatively high, and the $\mu\rho$ are relatively low.

The calculated elastic parameters can better reflect the physical properties of hydrate layers than the P-wave velocity, and the combination of multiple parameters can further reduce the multiplicity and improve the accuracy of quantitative interpretations and inversions. The method in this paper can provide a theoretical basis for quantitative calculations of hydrate saturation and also provides data guidance for quantitative interpretations of gas hydrates and optimizations of exploration areas.

6. Discussion and conclusions

Considering mineral composition, microstructure and the shear properties of hydrates, we built rock physical models

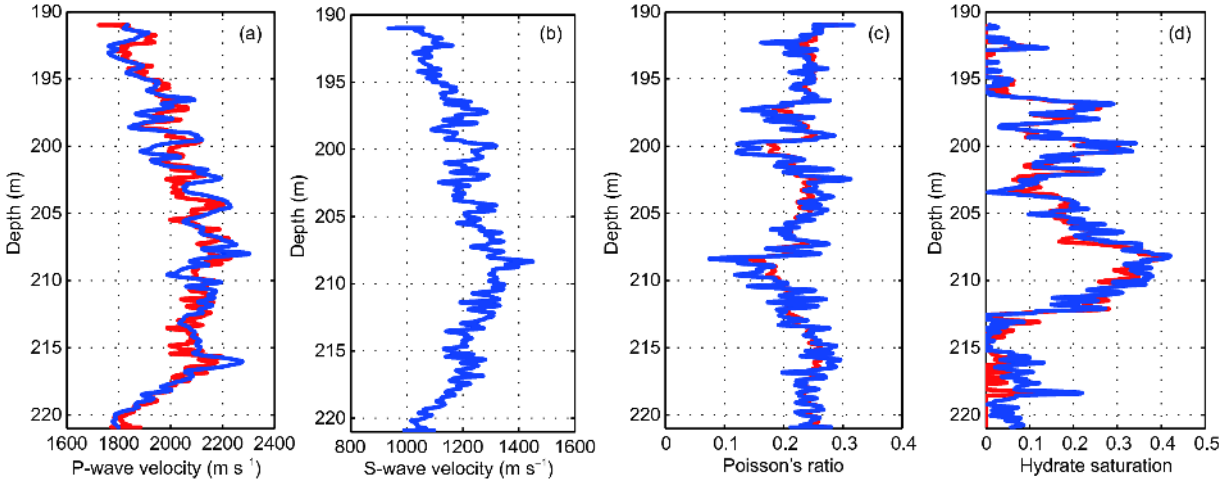

Figure 15 Calculated velocities, Poisson's ratio and hydrate saturation for the gas hydrate-bearing layer at site SH2. (a) V_P, the red solid line represents the measured values, and the blue solid line represents the calculated values; (b) calculated V_S; (c) Poisson's ratio, the red solid line represents the values calculated by the measured V_P and calculated V_S, and the blue solid line represents the values calculated by the calculated V_P and V_S; (d) hydrate saturation, the red solid line represents the hydrate saturation calculated using the Archie equation, and the blue solid line represents the hydrate saturation inverted from the calculated V_S.

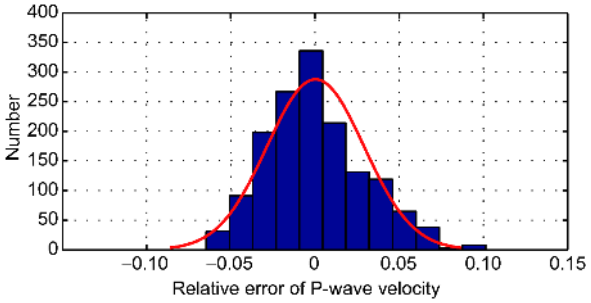

Figure 16 Relative errors of the calculated and measured values of P-wave velocity.

for load-bearing and pore-filling gas hydrate-bearing sediments under the theoretical framework of seismic rock physical modelling.

The rock physical models were applied to the laboratory data of Priest et al. (2005) and actual data from the Shenhu area in the North South China Sea, and good application results were obtained. The main advantages of the rock physical modelling method in this paper that distinguish it from previous methods are: (1) when considering the shape and connectivity of pores, the pore system is divided into poorly-connected penny-shaped pores and better-connected ellipsoidal pores, the DEM theory was used to quantitatively calculate the influence of microstructure of two kinds of pores on the elastic properties of the sediments, and (2) considering the shear properties of hydrates, the influence of hydrate components infilling pores on the elastic properties of the sediments is quantitatively calculated according to the generalized Gassmann theory.

On the one hand, the rock physical model established in this paper can provide information on elastic parameters, including S-wave velocity, Poisson' ratio and Lame parameters, which are lacking in conventional well logging, and provide data support for seismic quantitative interpretations and inversions, but on the other hand, physical parameters, including hydrate saturation and pore aspect ratio, can be obtained using measured data based on actual conditions, which provides a basis for quantitative descriptions and resource evaluations of gas hydrate-bearing reservoirs. The following conclusions and understandings were also obtained in the study.

(1) The P-wave and S-wave velocities decrease with increasing porosity and increase with increasing hydrate saturation. For hydrate formations with the same porosity, the P-wave and S-wave velocities of the LBGH formation are more sensitive to hydrate content. The P-wave and S-wave velocities both increase with PAR, and the P-S and P-wave velocities are more sensitive to hydrate saturation for smaller PARs. The P- and S-wave velocities increase with hydrate shear modulus, and velocities of the LBGH formations are more sensitive to the shear properties of the hydrates for formations with higher hydrate saturations.

(2) V_P/V_S decreases as porosity increases and hydrate saturation increases. When the porosity is low, the V_P/V_S of the PFGH formations increases slightly with hydrate saturation, whereas the V_P/V_S of the LBGH formations decreases slightly. When the porosity is high, the V_P/V_S of the LBGH formations decreases rapidly with hydrate saturation if the hydrate saturation is low and decreases slowly with hydrate saturation if the hydrate saturation is higher, and the V_P/V_S of the PFGH formations has an opposite variation trend. V_P/V_S of the PFGH formations is more sensitive to the presence of free gas, especially if the hydrate saturation is less than 20%, and the V_P/V_S of the PFGH formations is more easily affected by the shear properties of hydrates at higher hydrate saturations.

(3) $\lambda\rho$ and $\mu\rho$ have strong indicating ability to hydrate saturation, and the greater the porosity, the stronger the indicating ability. $\mu\rho$ has a strong indicating ability for hydrate saturation of the LBGH formations. When the porosity is low, the Poisson's ratios have stronger indicating ability to hydrate saturation of PFGH formations. When the porosity is high, Poisson's ratio has a stronger indicating ability to hydrate saturation of LBGH formations. The indicating abilities of $\lambda\rho$ and the Russell fluid factor are similar.

The application results for laboratory data and real data show the effectiveness of the rock physical methods. The

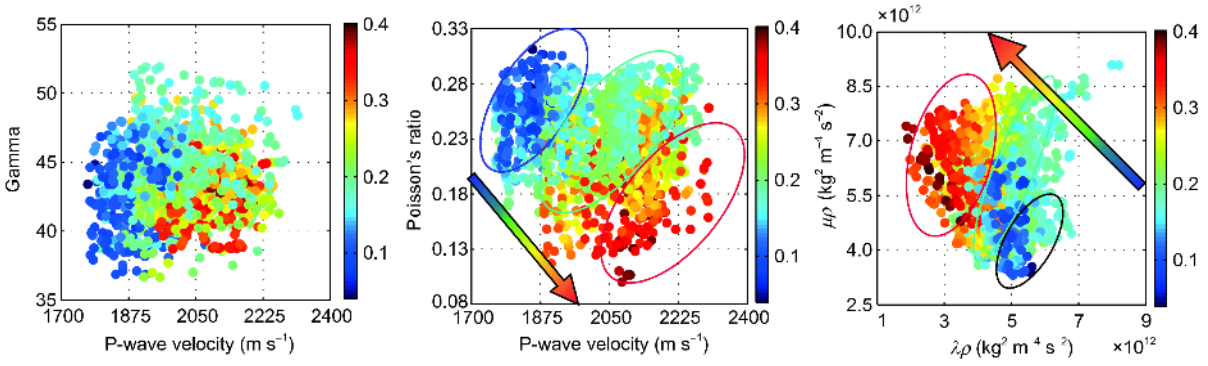

Figure 17 Crossplots of elastic parameters for gas hydrate-bearing sediments at site SH2. (a) Crossplot of measured V_P and Gamma; (b) crossplot of V_P and Poisson's ratio; (c) crossplot of $\lambda\rho$ and $\mu\rho$. The colorbars on the right of each crossplot represent hydrate saturation.

microstructure of a pore system can be described using different classification methods, and if the microstructure is very complex, it can be divided into many different pore types according to pore shape and connectivity. The pore aspect ratios and porosities of various pore types obtained in this paper are equivalent characterizations of the actual pore microstructure, which can reflect the composition and shape of the actual pores to some extent. The two models constructed in this paper assume that the gas hydrate-bearing formation is consolidated and that the solid components are homogeneous, elastic, and isotropic. The models do not consider the case of hydrates cementing solid mineral grains; the LBGH model assumes that hydrates are a solid component of the matrix, and the PFGH model assumes that hydrates are distributed in the pore spaces and have no mobility.

If the hydrates in the formation are partially deposited as solid grains and partially fill the pore spaces, the two models can be used in combination. In practical applications, if the input parameters are not known, on the one hand, empirical values of the parameters such as the elastic moduli of quartz and clay can be used, on the other hand, the parameters can be determined and calibrated based on measured data such as pore aspect ratio, and it is necessary to make more use of prior information, including well logging data such as P-wave velocity, density, and resistivity, core information, geochemical and seismic data in order to increase the accuracy of the input parameters and establish more accurate and reasonable rock physics models and provide powerful methods and data support for quantitative interpretations and predictions of gas hydrate-bearing reservoirs.

Acknowledgements *This study was supported by the National Natural Science Foundation of China (Grant No. 41706042), the China Postdoctoral Science Foundation (Grant No. 2015M582060), the Special Fund for Land & Resources Scientific Research in the Public Interest (Grant No. 201511037), the National Key Research and Development Program (Grant No. 2017YFC0307400) and the Foundation of Key Laboratory of Submarine Geosciences (Grant No. KLSG1603).*

References

Bai H, Pecher I A, Adam L, Field B. 2016. Possible link between weak bottom simulating reflections and gas hydrate systems in fractures and macropores of fine-grained sediments: Results from the Hikurangi Margin, New Zealand. Mar Pet Geol, 71: 225–237

Bao C. 1988. Natural Gas Geology. Beijing: Science Press (in Chinese). 390

Berge L I, Jacobsen K A, Solstad A. 1999. Measured acoustic wave velocities of R11 (CCl_3 F) hydrate samples with and without sand as a function of hydrate concentration. J Geophys Res, 104: 15415–15424

Berryman J G. 1995. Mixture theories for rock properties. AGU Reference Shelf, 3: 205–228

Brown R J S, Korringa J. 1975. On the dependence of the elastic properties of a porous rock on the compressibility of the pore fluid. Geophysics, 40: 608–616

Carcione J M, Tinivella U. 2000. Bottom-simulating reflectors: Seismic velocities and AVO effects. Geophysics, 65: 54–67

Carmichael R S. 1989. CRC Practical Handbook of Physical Properties of Rocks and Minerals. Florida: CRC Press. 741

Chand S, Minshull T A, Gei D, Carcione J M. 2004. Elastic velocity models for gas-hydrate-bearing sediments-a comparison. Geophys J Int, 159: 573–590

Chen Y F, Li D L, Liang D Q, Zhou X B, Wu N Y. 2013. Relationship between gas hydrate saturation and resistivity in sediments of the South China Sea. Acta Petrol Sin (in Chinese), 34: 507–512

Ciz R, Shapiro S A. 2007. Generalization of Gassmann equations for porous media saturated with a solid material. Geophysics, 72: A75–A79

Dai J, Xu H, Snyder F, Dutta N. 2004. Detection and estimation of gas hydrates using rock physics and seismic inversion: Examples from the northern deepwater Gulf of Mexico. Lead Edge, 23: 60–66

Dallimore S R, Collett T S, Uchida T. 1999. Overview of science program, JAPEX/JNOC/GSC Mallik 2L-38 gas hydrate research well. Bull Geol Surv Can, 544: 11–17

Dillon W P, Lee M W, Fehlhaber K, Coleman D F. 1993. Gas hydrates on the Atlantic continental margin of the United States. US Geological Survey Professional Paper, 1570: 313–330

Dun T J. 1995. Reservoir research status and development trend (in Chinese). Northwest Geol, 16: 1–15

Dutta N C, Dai J. 2009. Exploration for gas hydrates in a marine environment using seismic inversion and rock physics principles. Leading Edge, 28: 792–802

Dvorkin J, Nur A. 1993. Rock Physics for characterization of gas hydrates. US Geological Survey Professional Paper, 1570: 293–298

Dvorkin J, Nur A. 1996. Elasticity of high-porosity sandstones: Theory for two North Sea data sets. Geophysics, 61: 1363–1370

Dvorkin J, Prasad M. 2001. Velocity to porosity transform in marine sediments. Petrophysics, 42: 429–437

Ecker C. 2001. Methane hydrate rock physics models for the Blake Outer Ridge. Stanford Exploration Project, 80: 1–18

Ecker C, Dvorkin J, Nur A. 1998. Sediments with gas hydrates: Internal structure from seismic AVO. Geophysics, 63: 1659–1669

Ecker C, Dvorkin J, Nur A M. 2000. Estimating the amount of gas hydrate and free gas from marine seismic data. Geophysics, 65: 565–573

Gassmann F. 1951. Elastic Waves through a packing of spheres. Geophysics, 16: 673–685

Gao H Y, Zhong G F, Liang J Q, Guo Y Q. 2012. Estimation of gas hydrate saturation with modified Biot-Gassmann theory: A case from northern South China Sea. Mar Geol Quat Geol, 32: 83–89

Helgerud M B, Dvorkin J, Nur A, Sakai A, Collett T. 1999. Elastic-wave velocity in marine sediments with gas hydrates: Effective medium modeling. Geophys Res Lett, 26: 2021–2024

Helgerud M B, Waite W F, Kirby S H, Nur A. 2009. Elastic wave speeds and moduli in polycrystalline ice Ih, sI methane hydrate, and sII methane-ethane hydrate. J Geophys Res, 114: B02212

Hill R. 1963. Elastic properties of reinforced solids: Some theoretical principles. J Mech Phys Solids, 11: 357–372

Holbrook W S, Hoskins H, Wood W T, Stephen R A, Lizarralde D, Leg 164 Science Party D. 1996. Methane hydrate and free gas on the blake ridge from vertical seismic profiling. Science, 273: 1840–1843

Hu G W, Li C F, Ye Y G, Liu C L, Zhang J, Diao S B. 2014. Observation of gas hydrate distribution in sediment pore space (in Chinese). Chin J Geophys, 5: 1675–1682

Jakobsen M, Hudson J A, Minshull T A, Singh S C. 2000. Elastic properties of hydrate-bearing sediments using effective medium theory. J Geophys Res, 105: 561–577

Jiang Z X. 2003. Sedimentology (in Chinese). Beijing: Petroleum Industry Press. 180–197

Jin S, Nagao J, Takeya S, Jin Y, Hayashi J, Kamata Y, Ebinuma T, Narita H. 2006. Structural investigation of methane hydrate sediments by microfocus X-ray computed tomography technique under high-pressure conditions. Jpn J Appl Phys, 45: L714–L716

Kleinberg R L, Flaum C, Griffin D D, Brewer P G, Malby G E, Peltzer E T, Yesinowski J P. 2003. Deep sea NMR: Methane hydrate growth habit in porous media and its relationship to hydraulic permeability, deposit accumulation, and submarine slope stability. J Geophys Res, 108: 2508

Kvenvolden K A. 1993. A primer of gas hydrates. US Geological Survey Professional Paper, 1570: 555–561
Lee M W, Collett T S. 2001. Elastic properties of gas hydrate-bearing sediments. Geophysics, 66: 763–771
Lee M W, Hutchinson D R, Collett T S, Dillon W P. 1996. Seismic velocities for hydrate-bearing sediments using weighted equation. J Geophys Res, 101: 20347–20358
Lee M W, Waite W F. 2008. Estimating pore-space gas hydrate saturations from well log acoustic data. Geochem Geophys Geosyst, 9: Q07008
Li W X, Wang H, Yao Z X, Liu Y K, Chang X. 2009. Shear-wave velocity estimation and fluid substitution by constraint method (in Chinese). Chin J Geophys, 52: 785–791
Liu C L, Ye Y G, Meng Q G, He X L, Cheng Q, Hu G W. 2012. Characteristics of gas hydrate samples recovered from Shenhu Area in the South China Sea (in Chinese). J Trop Oceanogr, 31: 1–5
Liu J, Liu J P, Cheng F, Wang J, Liu X X. 2017. Rock-physics models of hydrate-bearing sediments in permafrost, Qilian Mountains, China. Appl Geophys, 14: 31–39
Liu X W, Li M F, Zhang Y W, Zhang G X, Wu N Y, Huang Y Y, Wang H B.. 2005. Studies of seismic characteristics about gas hydrate: A case study of line HDl52 in the South China Sea (in Chinese). Geol Sci, 19: 33–38
Lu H, Seo Y T, Lee J W, Moudrakovski I, Ripmeester J A, Chapman N R, Coffin R B, Gardner G, Pohlman J. 2007. Complex gas hydrate from the Cascadia margin. Nature, 445: 303–306
Lu H F, Chen H, Chen F, Liao Z L. 2009. Mineralogy of the sediments from gas-hydrate drilling sites, Shenhu area, South China Sea (in Chinese). Research of Eological South China Sea, 20: 28–39
Lu S M, McMechan G A. 2002. Estimation of gas hydrate and free gas saturation, concentration, and distribution from seismic data. Geophysics, 67: 582–593
Luan X W, Jin Y K, Obzhirov A, Yue B J. 2008. Characteristics of shallow gas hydrate in Okhotsk Sea. Sci China Ser D-Earth Sci, 51: 415–421
Mason W P. 1943. Chapter I: Quartz crystal applications. Bell Syst Technical J, 22: 178–223
Mavko G, Mukerji T, Dvorkin J. 2009. The Rock Physics Handbook: Tools for Seismic Analysis in Porous Media. 2nd ed. New York: Cambridge University Press
Miller J J, Lee M W, von Huene R. 1991. An analysis of a seismic reflection from the base of a gas hydrate zone, Offshore Peru. AAPG Bull, 75: 910–924
Priest J A, Best A I, Clayton C R I. 2005. A laboratory investigation into the seismic velocities of methane gas hydrate-bearing sand. J Geophys Res, 110: B04102
Qian J, Wang X J, Dong D D, Wu S G, Sain K, Ye Y M. 2016. Quantitative assessment of free gas beneath gas hydrate stability zone from prestack seismic data and rock physics: A case of hole NGHP01-10A, Krishna-Godava basin, India (in Chinese). Chin J Geophys, 59: 2553–2563
Qu L, Zou C C, Lu Z Q, Yu C Q, Li N, Zhu J C, Zhang X H, Yue X Y, Gao M Z. 2017. Elastic-wave velocity characterization of gas hydrate-bearing fractured reservoirs in a permafrost area of the Qilian Mountain, Northwest China. Mar Pet Geol, 88: 1047–1058
Russell B H, Hedlin K, Hilterman F J, Lines L R. 2003. Fluid-property discrimination with AVO: A Biot-Gassmann perspective. Geophysics, 68: 29–39
Sakai A. 1999. Velocity analysis of vertical seismic profile (VSP) survey at JAPEX/JNOC/GSC Mallik 2L-38 gas hydrate research well, and related problems for estimating gas hydrate concentration. Bull Geol Surv Can, 544: 323–340
Sava D, Hardage B A. 2006. Rock physics characterization of hydrate-bearing deepwater sediments. Leading Edge, 25: 616–619
Schultheiss P, Holland M, Humphrey G. 2009. Wireline coring and analysis under pressure: Recent use and future developments of the HYACINTH system. Sci Dril, 7: 44–50
Shankar U, Riedel M. 2011. Gas hydrate saturation in the Krishna-Godavari basin from *P*-wave velocity and electrical resistivity logs. Mar Pet Geol, 28: 1768–1778
Shipley T H, Houston M H, Buffler R T, Shaub F J, McMillen K J, Ladd J W, Worzel J L. 1979. Seismic evidence for widespread possible gas hydrate horizons on continental slopes and rises. AAPG Bull, 63: 2204–2213
Song H B, Osamu M, Yang S X, Wu N Y, Jiang W W, Hao T Y. 2002. Physical property models of gas hydrate-bearing sediments and AVA character of bottom simulating reflector (in Chinese). Chin J Geophys, 45: 546–556
Song H B, Wu S G, Jiang W W. 2007. The characteristics of BSRs and their derived heat flow on the profile 973 in the northeastern South China Sea (in Chinese). Chin J Geophys, 50: 1508–1517
Tohidi B, Anderson R, Clennell M B, Burgass R W, Biderkab A B. 2001. Visual observation of gas-hydrate formation and dissociation in synthetic porous media by means of glass micromodels. Geology, 29: 867–870
Tosaya C, Nur A. 1982. Effects of diagenesis and clays on compressional velocities in rocks. Geophys Res Lett, 9: 5–8
Waite W F, Helgerud M B, Nur A, Pinkston J C, Stern L A, Kirby S H, Durham W B. 2000. Laboratory measurements of compressional and shear wave speeds through methane hydrate. Ann New York Acad Sci, 912: 1003–1010
Waite W F, Santamarina J C, Cortes D D, Dugan B, Espinoza D N, Germaine J, Jang J, Jung J W, Kneafsey T J, Shin H, Soga K, Winters W J, Yun T S. 2009. Physical properties of hydrate-bearing sediments. Rev Geophys, 47: 465–484
Wang J, Sain K, Wang X, Satyavani N, Wu S. 2014. Characteristics of bottom-simulating reflectors for Hydrate-filled fractured sediments in Krishna-Godavari basin, eastern Indian margin. J Pet Sci Eng, 122: 515–523
Wang J, Zhao J, Zhang Y, Wang D, Li Y, Song Y. 2016. Analysis of the effect of particle size on permeability in hydrate-bearing porous media using pore network models combined with CT. Fuel, 163: 34–40
Wang X, Hutchinson D R, Wu S, Yang S, Guo Y. 2011. Elevated gas hydrate saturation within silt and silty clay sediments in the Shenhu area, South China Sea. J Geophys Res, 116: B05102
Wang Y, Chen S, Wang L, Li X Y. 2013. Modeling and analysis of seismic wave dispersion based on the rock physics model. J Geophys Eng, 10: 054001
Weger R J, Eberli G P, Baechle G T, Massaferro J L, Sun Y F. 2009. Quantification of pore structure and its effect on sonic velocity and permeability in carbonates. AAPG Bull, 93: 1297–1317
Westbrook G K, Chand S, Rossi G, Long C, Bünz S, Camerlenghi A, Carcione J M, Dean S, Foucher J P, Flueh E, Gei D, Haacke R R, Madrussani G, Mienert J, Minshull T A, Nouzé H, Peacock S, Reston T J, Vanneste M, Zillmer M. 2008. Estimation of gas hydrate concentration from multi-component seismic data at sites on the continental margins of NW Svalbard and the Storegga region of Norway. Mar Pet Geol, 25: 744–758
Winters W J, Dallimore S R, Collett T S, Katsube T J, Jenner K A, Cranston R E, Wright J F, Nixon F M, Uchida T. 1999. Physical properties of sediments from the JAPEX/JNOC/GSC Mallik 2L-38 gas hydrate research well, determined using Gas Hydrate And Sediment Test Laboratory Instrument (GHASTLI). Bull Geol Surv Can, 544: 95–100
Winters W J, Waite W F, Mason D H, Gilbert L Y, Pecher I A. 2007. Methane gas hydrate effect on sediment acoustic and strength properties. J Pet Sci Eng, 56: 127–135
Wood W T, Stoffa P L, Shipley T H. 1994. Quantitative detection of methane hydrate through high-resolution seismic velocity analysis. J Geophys Res, 99: 9681–9695
Wu N Y, Yang S X, Wang H B, Liang J Q, Gong Y H, Lu Z Q, Wu D D, Guan H X. 2009. Gas-bearing fluid influx sub-system for gas hydrate geological system in Shenhu area, northern South China Sea (in Chinese). Chin J Geophys, 52: 1641–1650
Xu S Y, White R E. 1995. A new velocity model for clay-sand mixtures. Geophys Prospect, 43: 91–118
Xue J, Gu H M, Cai C G, Li Z J, Zhu D. 2016. Estimation of fracture

parameters from P-wave AVOA data based on equivalent media theory (in Chinese). Oil Geophys Prosp, 51: 1171–1179
Ye Y G, Liu C L. 2011. Experimental Techniques and Their Applications for Natural Gas Hydrates (in Chinese). Beijing: Geological Publishing House. 88–89
Yin X Y, Hua S B, Zong Z Y. 2016. A decoupling approach for differential equivalent equations based on linear approximation (in Chinese). Oil Geophys Prosp, 51: 281–287
Yin X Y, Liu X X. 2016. Research status and progress of the seismic rock-physics modeling methods (in Chinese). Geophys Prosp Petrol, 55: 309–325
Yin X Y, Zong Z Y, Wu G C. 2015. Research on seismic fluid identification driven by rock physics. Sci China Earth Sci, 58: 159–171
Zimmerman R W, King M S. 1986. The effect of the extent of freezing on seismic velocities in unconsolidated permafrost. Geophysics, 51: 1285–1290

(Responsible editor: Dinghui YANG)